ARTICLE

Real-time impedance-activated dielectrophoretic actuation for reconfigurable manipulation of single flowing particles

Alexis Lefevre,[a,†] Cristian Brandi,[b,†] Adele De Ninno,[c] Filippo Ruggiero,[c] Enrico Verona,[c] Michaël Gauthier,[a] Paolo Bisegna,[b] Aude Bolopion[a] and Federica Caselli[b,*]

This work presents an innovative all-electrical platform for selective single-particle manipulation. The platform combines microfluidic impedance cytometry for label-free particle characterization and dielectrophoresis for contactless multi-way particle separation. The microfluidic chip has a straightforward coplanar electrode layout and no particle pre-focusing mechanism is required. An original online algorithm analyzes the impedance signals of each incoming particle and regulates in real-time the dielectrophoretic voltages according to a desired control logic. As proof-of-concept, three operation modes are demonstrated on a mixture of 8, 10, and 12 µm diameter beads: (i) particle position swapping across channel axis, irrespective of particle size, (ii) size-based particle separation, irrespective of particle position, and (iii) sorting of a selected sequence of particles. As a perspective, the versatility of impedance cytometry and dielectrophoresis and the possibility to configure alternative control logics hold promises for advanced particle and cell manipulation.

1 Introduction

Precise and selective manipulation of both synthetic and biological particles has long been motivated by applications in materials science, physics, and life sciences.[1] Examples include particle separation from complex mixtures, control of microrobots, and creation of particle assemblies. A system for particle manipulation generally requires three main components: (i) a sensor, to characterize particle properties, (ii) an actuator, to move selected particles at designated places, and (iii) a control centre that instructs the actuator based on the signals perceived from the sensor. Besides features such as low-cost and ease of use, desirable system features include label-free sensing and contactless actuation. To build such a system, microfluidics coupled with active force fields (e.g., optic, acoustic, or electric fields) offers powerful and diverse opportunities.[2] A thorough discussion of microfluidic approaches for particle manipulation can be found e.g. in Refs.[2–8]

A common manipulation task is separation and sorting of flowing particles. Most frequently this consists in a two-way sorting task where target particles are deviated to a collection outlet while non-target particles flow unperturbed towards the waste outlet. Generally, particles are pre-focused before reaching the sorting region. Ai's group recently demonstrated a microfluidic system for acoustic single-cell sorting activated by microfluidic impedance cytometry[9] (MIC) characterization. They reported applications to sorting of live cells from a mixture of fixed and live cells,[10] viability enrichment of cryopreserved cells,[11] and selectable encapsulated cell quantity in droplets[12,13]. Dielectrophoretic separation and sorting has also been widely used[14–17]. While dielectrophoresis (DEP) is generally used for bulk sorting of particle/cell populations,[18–22] a few DEP-based system with single-particle resolution have been reported. de Wagenaar et al.[23] reported a system for two-way sorting, based on MIC characterization and DEP actuation, and demonstrated online separation of beads from sperm cells. Thomas et al.[24] combined fluorescence imaging and DEP actuation. A nice feature of that approach is the introduction of "dielectrophoretic virtual channel": by switching the polarity of the electrodes, the virtual channel can be dynamically reconfigured to direct particles along a different path. The concept of reconfigurable microfluidics is indeed an intriguing and promising direction.[25]

Compared to other sorting approaches, DEP offers the possibility for precise control of particle trajectory[26,27] thus enabling multi-way sorting. Lipp et al. recently exploited this feature to implement the controlled contact between single micro-sized objects[28] and the formation of aggregates of controlled size and composition[29]. However, a present limitation of those systems[28,29] is the lack of full automation.

a. Université de Franche-Comté, CNRS, SUPMICROTECH, Institute FEMTO-ST, F25000 Besançon, France
b. Department of Civil Engineering and Computer Science, University of Rome Tor Vergata, Rome, Italy. E-mail: caselli@ing.uniroma2.it
c. Italian National Research Council – Institute for Photonics and Nanotechnologies (CNR - IFN), Rome, Italy
† These authors contributed equally to this work.
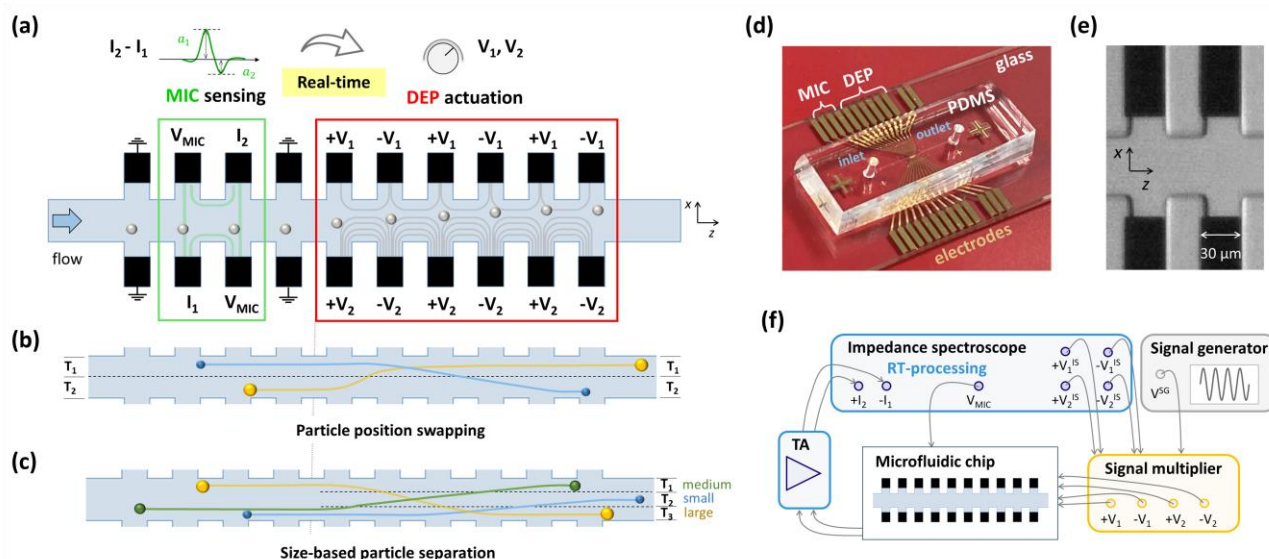
Fig. 1 (a) Schematic representation of the working principle of the system. Individual flowing particles are characterized via MIC sensing (green box). The measured differential current ($I_2 - I_1$) is processed in real time to regulate the voltages V_1 and V_2 of the DEP actuation region (red box). (b) Particle position swapping. (c) Size-based particle separation. (d) Photograph of the microfluidic chip. (e) Microscopy image of the MIC sensing zone. (f) Overall system electrical connections (RT, real-time, TA, transimpedance amplifier).

This work presents an innovative all-electrical microfluidic platform for automatic, precise, and selective manipulation of individual flowing particles. As detailed in Section 2, the system leverages MIC-sensing for label-free particle characterization and DEP-actuation for particle trajectory control. Contactless manipulation approaches, such as DEP-actuation, reduce the risks of contamination and of damaging fragile particles[30] and avoid issues arising from the inertia of manipulators[31]. As presented in Section 3, an original real-time processing and control algorithm is developed, to regulate the DEP-actuation based on MIC-sensing. In Section 4, three control logics are programmed, thus enabling different separation tasks. Specifically, we demonstrate experimentally particle position swapping, size-based particle separation, and sorting of a selected particle sequence, on particles of 8 to 12 µm diameter, without requiring any particle pre-focusing stage. This versatile and reconfigurable platform is therefore a promising tool for advanced separation and sorting applications.

2 Device working principle

The working principle of the proposed system is illustrated in Fig. 1. The microfluidic chip is composed of two subsequent regions: a sensing region based on MIC (Microfluidic Impedance Cytometry) and an actuation region based on DEP. The overall layout is straightforward and consists of a main channel with rectangular cross section and ten pairs of dead-end lateral chambers, which house coplanar electrodes on their floor (Fig.1(a)). The MIC-based sensing region spans two electrode pairs (i.e., 2nd and 3rd from the left), while six electrode pairs (from 5th to 10th) are used for DEP-based manipulation. The electrode pair between the MIC region and the DEP region (i.e., the 4th one) is grounded, to mitigate possible cross-talks between sensing and actuation signals. The first electrode pair

is grounded too, to ensure symmetric conditions before and after the MIC region.

The layout and the wiring scheme of the MIC region[32] allow to obtain electrical signals that provide: (i) an electrical estimate of particle lateral position (i.e., along the x-axis in Fig.1(a)),[33,34] and (ii) an accurate characterization of particle properties (i.e., size).[35] Briefly, an AC voltage (V_{MIC}) is applied to diagonally opposite electrodes and the differential current ($I_2 - I_1$) from the remaining electrodes is acquired (Fig.1(a), green box). Upon the passage of a flowing particle, the measured current exhibits an asymmetric bipolar Gaussian shape, characterized by positive and negative pulses with generally different peak amplitudes (a_1 and a_2). As detailed in Refs.[32,33], the relative difference of peak amplitudes

$$\Delta = \frac{a_2 - a_1}{(a_2 + a_1)/2} \tag{1}$$

correlates with particle lateral position. The larger Δ the larger particle's lateral off-centring, and the sign of Δ depends on the off-centring side with respect to the main channel axis (i.e., positive/negative x-coordinate). Besides providing information on particle trajectory, the metric Δ enables an accurate electrical estimate of particle size, despite the position-induced blurring associated to field non-uniformity.[35] Specifically, denoting by a the mean peak amplitude

$$a = (a_1 + a_2)/2 \tag{2}$$

an accurate estimate of particle diameter is given by:

$$D\text{-corr} = \frac{D}{[1 + b(\Delta - c)^2]} \tag{3}$$

where

$$D = G|a|^{1/3} \tag{4}$$

is the raw estimate of particle diameter and G, b, and c are calibration coefficients (see also Section 4.3).

The wiring scheme of the DEP region was introduced in Refs.[36,37] to achieve controlled lateral deviation of particles in liquid flows. Voltages V_1 and V_2 are applied to the electrodes on opposite sides of the channel, with π phase-shift among even and odd pairs (Fig. 1(a), red box). The resulting electric field is such that particles experiencing negative DEP (nDEP) are displaced toward an equilibrium position. By adjusting the ratio of the applied voltages V_1 and V_2 the equilibrium position can be swept across the channel width (i.e., the x-axis). Specifically, for $V_1 > V_2$ the equilibrium position is in the bottom half of the channel ($x < 0$), for $V_2 > V_1$ the equilibrium position is in the top half of the channel ($x > 0$), while equal voltages induce particle focusing along channel axis (see also Section 4.1).

To achieve selective particle manipulation, the differential signal acquired from the MIC region is processed in real time to extract the properties (e.g., lateral position, size) of the current particle and to set the DEP voltages accordingly (see also Section 3.4). Several control logics can be implemented. In this work, we present three proof-of-concept actuation modes: particle position swapping, size-based particle separation, and sorting of a selected particle sequence.

In particle position swapping (Fig. 1(b)), the width of the channel is conceptually divided into two tracks (T_1 and T_2) and each flowing particle is moved to the opposite track with respect to its entrance one. In other words, particles passing through the MIC sensing region along the top track T_1 are displaced to the bottom track T_2, and vice versa. This is done irrespectively of particle size.

In size-based particle separation (Fig. 1(c)), the exit region of the main channel is conceptually divided into tracks and particles are displaced to a specific track depending on their size. Specifically, here we consider three particle sizes and corresponding tracks: small size particles are moved to the central track (T_2), medium size particles are moved to the top track (T_1), and large size particles are moved to the bottom track (T_3). This is done irrespective of particle entrance position.

Finally, in the sorting of a selected particle sequence, desired particles are moved to a "target" track (T_1) whereas out-of-sequence particles are moved to a "waste" track (T_2) (see also Fig. 6 of Section 4.4).

3 Materials and Methods

3.1 Microfluidic impedance chip

The microfluidic impedance chip consists of a PDMS block, housing the microchannel, bonded to a glass slide with patterned gold electrodes (Fig. 1(d) and (e)). The chip was fabricated following standard processes described in previous works[33,38]. To mitigate possible electrode corrosion mechanisms associated to the applied DEP voltages, the electrodes were passivated with a layer of SiO_2 (~40 nm). Chip

dimensions are as follows: the main channel is 50 μm wide and 21.5 μm high; the ten lateral channels are 30 μm wide with a 60 μm pitch; the electrodes in the lateral channels are recessed by 15 μm with respect to the main channel. Prior to impedance data collection, the microfluidic chip was flushed with a 1% BSA (bovine serum albumin) solution in PBS to prevent particle adhesion to the PDMS walls.

3.2 Sample preparation

Polystyrene beads (Supelco) of 8, 10, or 12 μm diameter were suspended at a concentration of 10^6 beads per mL in 1× PBS buffer augmented with 13% sucrose. The addition of sucrose brings the buffer density close to that of the beads (1.05 g/mL), thus mitigating particle sedimentation. Moreover, it reduces buffer conductivity to 0.9 S/m, which turned out to be suitable for both MIC sensing and DEP actuation. A mixed sample containing the three bead populations in equal proportion was prepared and used in the experimental tests. The sample was loaded into a syringe pump (Elite 11, Harvard Apparatus, with 250 μL syringe) and pumped into the microfluidic chip at 100 nL/min.

3.3 MIC signal acquisition and generation of DEP voltages

Figure 1(f) shows an overview of the system connections. The AC voltage V_{MIC} (6 V at 3 MHz) is generated by an impedance spectroscope (HF2IS with RT-option, Zurich Instruments). The measured currents I_1 and I_2 are conditioned by a transimpedance amplifier (HF2TA, Zurich Instruments, 10 kΩ gain) and the differential current ($I_2 - I_1$) is demodulated by the spectroscope (1.8 kHz sampling rate, 100 Hz bandwidth). The demodulated signal is processed in real-time with a custom C-script running on the embedded RISC microprocessor (cf. Section 3.4). According to the properties of the current particle and the desired actuation mode, DC signals are generated at the auxiliary outputs of the HF2IS spectroscope (V_1^{IS}, $-V_1^{IS}$, V_2^{IS}, $-V_2^{IS}$). By using a custom-made signal multiplier, the latter signals are multiplied by a sinusoidal waveform V^{SG} (1.5 V amplitude, 400 kHz frequency) generated by a signal generator (KeySight 33500B), thus obtaining the DEP voltages V_1 and V_2 and their phase-shifted versions $-V_1$ and $-V_2$.

For offline validation purposes, the demodulated signal is recorded by the HF2IS during the acquisitions as well as the DC signal V_1^{IS}.

3.4 Real-time signal processing and control

The original real-time signal processing and control algorithm, written in C language, is based on a finite-state machine. The initial state is "S_0: Wait for new event". The other states are "S_1: Find peaks" and "S_2: Refractory".

The main loop of the algorithm is run at the sampling frequency of 1.8 kHz. At each iteration, a new signal sample is acquired from the demodulator (raw signal s_R, Fig. 2(a)). Its moving

Fig. 2 (a) Exemplary portion of the raw signal (s_R) recorded from the MIC sensing zone upon the passage of a particle (i.e., real part of the demodulated differential signal at 3 MHz). The event signal exhibits an asymmetric bipolar shape. (b) Intermediate outcomes of the real-time signal processing algorithm, namely, the high pass filtered signal (s_F) and the derived signal (s_{ED}) that is used for event detection. The event detection threshold (T_{ED}) and the corresponding state are also shown.

(a)

(b)
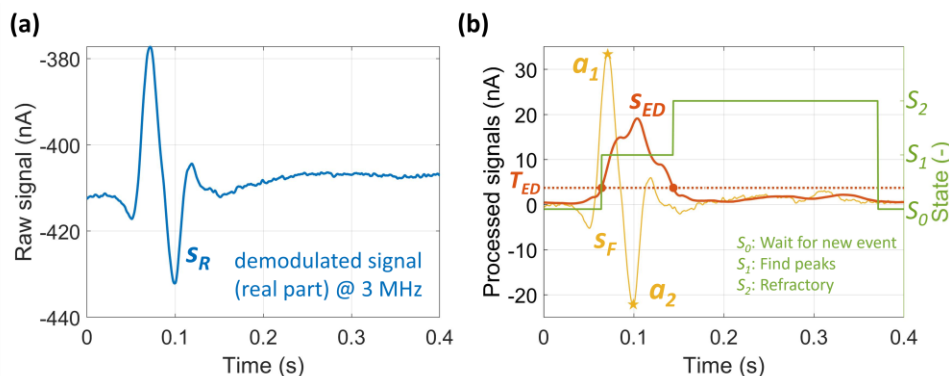
average is updated and subtracted from s_R, thus removing the baseline and obtaining the high-pass filtered signal s_F (Fig. 2(b), yellow line). The moving average of the absolute value of s_F is then updated, yielding the processed signal s_{ED} which is suitable for event detection (Fig. 2(b), red line). In fact, a particle passing through the measuring zone, reflected by the bipolar shape in the raw signal s_R, produces a single pulse in the signal s_{ED}.

As the magnitude of s_{ED} becomes larger than a threshold T_{ED}, the state (Fig. 2(b), green line) changes from "S_0: Wait for new event" to "S_1: Find peaks". In the latter state, the signal peak amplitudes a_1, a_2 are computed. Then, as the magnitude of s_{ED} returns below the threshold T_{ED}, the state changes to "S_2: Refractory". In this state, any upcoming event is neglected to avoid interference from particles coming in immediately afterwards. Finally, after a fixed period, the state returns to "S_0: Wait for new event".

The signal s_{ED} used for triggering state transitions is slightly delayed with respect to the signal s_F (cf. Fig 2(b)), due to the moving average operation. Although the peak detection task is performed on s_F during state "S1: Find peaks", a correct peak detection is accomplished because the latest samples of s_F are stored.

At the transition from state "S_1: Find peaks" to state "S_2: Refractory", the peak amplitudes a_1, a_2 are available and are used to compute the electrical metric Δ (eq. (1)), which encodes particle lateral position, and the corrected electrical diameter D-corr (eq. (3)). The DC voltages at the auxiliary outputs of the impedance spectroscope (V_1^{IS}, $-V_1^{IS}$, V_2^{IS}, $-V_2^{IS}$) are therefore updated at the S_1 to S_2 transition based on the desired operation mode (cf. Sections 4.2, 4.3 and 4.4).

3.5 Matlab replica of the real-time algorithm

Besides the C-version of the signal processing and control algorithm, running on the RISC microprocessor of the HF2IS, a Matlab replica of the algorithm was implemented to run offline for validation and calibration purposes (cf. Section 4.3). The Matlab algorithm loads the recorded demodulated signal and allows to recreate all the intermediate signal processing variables and the resulting DC voltages. The replicated voltage V_1^{IS} is identical to the recorded one, thus confirming that the Matlab algorithm is an accurate replica of the C algorithm. Moreover, assuming as gold standard for the event-detection

the results of a traditional correlation-based algorithm[39], the finite-state machine algorithm achieved a sensitivity of 95% and a positive predictive value of 98%.

3.6 Image data acquisition and processing

Simultaneously to impedance measurements, the sample flow through the sensing region was imaged with a high-speed camera (Photron, Mini UX100)[40]. The frame rate was set to 50 fps, with shutter time 20 ms. A hardware link allowed synchronization of impedance data and video recordings. A custom Matlab script was used to implement particle tracking across the image frames. It is emphasized that the camera is only used to record the process for validation purpose, but it is not involved in the control.

3.7 Finite element model

A 3D finite element model of the device was implemented, to obtain the distribution of the electric potential within the microchannel and derived quantities (namely, the DEP force). Details of model equations can be found in previous literature (e.g., Ref.[41]). The parameter values used in the numerical simulations are as follows: medium conductivity 0.9 S/m, medium relative permittivity 80, bead conductivity 6.7×10^{-4} S/m, bead relative permittivity 2.5, bead diameter 10 μm, electrode double layer capacitance 14.4×10^{-2} F/m^2, DEP voltage frequency 400 kHz. The resulting value of the Clausius-Mossotti factor is about -0.5 (see also Section 4.1 and Fig. S1 of the Supplementary Material).
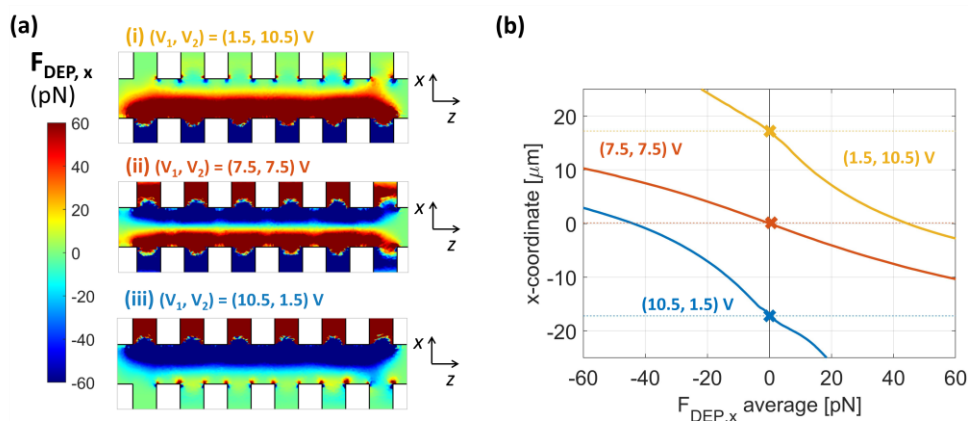
Fig. 3 Finite element simulation results for three different values of the DEP voltages: $(V_1, V_2) = (1.5,10.5)$ V, $(V_1, V_2) = (7.5,7.5)$ V, and $(V_1, V_2) = (10.5,1.5)$ V. (a) Distribution of the x-component of the DEP force $(F_{DEP,x})$ at channel mid height, (b) Average value of $F_{DEP,x}$ along channel length (i.e., along the z-coordinate), as a function of the position along channel width (i.e., x-coordinate). The equilibrium position (i.e., x-coordinate at null force) is highlighted with a cross.

4 Results

4.1 Finite element computation of the DEP force

The (time-averaged) dielectrophoretic force acting on a polarizable particle in a nonhomogeneous electric field is given by:[42]

$$\boldsymbol{F}_{DEP} = 2\pi r^3 \varepsilon_m \text{Re}[K(\omega)]\nabla|E_{rms}|^2$$

where E_{rms} is the root-mean-square electric field, r is the particle radius, ω is the angular field frequency, ε_m is the relative permittivity of the medium, and $\text{Re}[K(\omega)]$ indicates the real part of the Clausius-Mossotti factor $K(\omega)$. The latter is given by:

$$K(\omega) = \frac{\varepsilon_p^* - \varepsilon_m^*}{\varepsilon_p^* + 2\varepsilon_m^*}$$

where ε_p^* and ε_m^* are the complex permittivities of the particle and the medium, respectively.

Three different actuation voltage pairs were considered in simulation: (i) $(V_1, V_2) = (1.5,10.5)$ V, (ii) $(V_1, V_2) = (7.5,7.5)$ V, and (iii) $(V_1, V_2) = (10.5,1.5)$ V. Fig. 3(a) shows the distribution over the channel middle height of the x-component of the DEP force, $F_{DEP,x}$, and Fig. 3(b) shows its average along z. As expected, particles undergoing nDEP will be accordingly moved towards the top (positive x), the center ($x = 0$), and the bottom (negative x) for DEP voltages (1.5,10.5) V, (7.5,7.5) V, and (10.5,1.5) V, respectively.
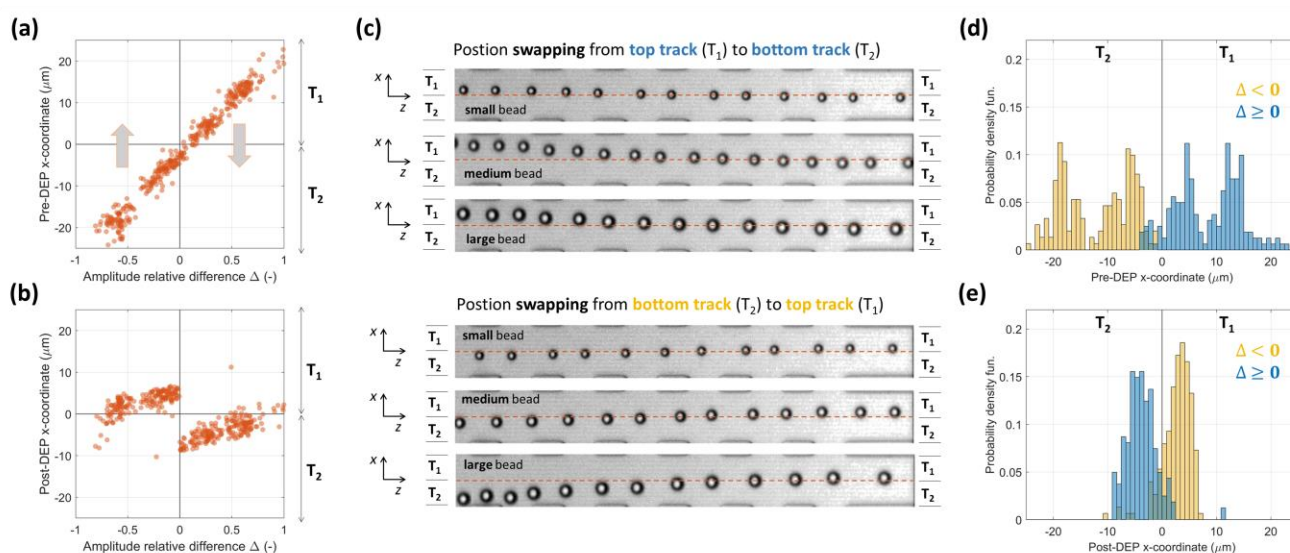
4.2 Operation mode 1: particle position swapping

The system functionality was first tested by running the particle position swapping experiment (Fig. 1(b)). This experiment requires real-time estimation of particle x-coordinate before the DEP actuation region. Such x-coordinate is encoded by the relative difference of the pulse amplitudes of the MIC signal, i.e. by the electrical metric Δ (eq. (1)). This was verified by comparison with image processing results. Specifically, Fig. 4(a) reports the scatter plot of the pre-DEP optical x-coordinate of

particle centre against Δ. The former was obtained via particle tracking, while the latter was reconstructed with the Matlab replica of the online signal processing algorithm. As expected, they are proportional to each other, which confirms that Δ can be used as an estimate of particle position. In particular, particles with negative Δ are traveling along the bottom track T_2 (negative x-coordinate), whereas particles with positive Δ are traveling along the top track T_1 (positive x-coordinate).

To achieve particle position swapping, the following control logic is therefore implemented: if Δ is negative (track T_2), the DC voltages (V_1^{IS}, V_2^{IS}) are set to $(1,7)$ V, thus yielding DEP voltages $V_1 = V_1^{IS}V^{SG} = 1.5$ V and $V_2 = V_2^{IS}V^{SG} = 10.5$ V, and hence pushing the particle towards the top half of the microchannel (track T_1). Vice versa, if Δ is positive, the DC voltages are set to $(7,1)$ V. This operation mode effectively swaps particle tracks (Fig. 4(b)): after the DEP actuation region, particles with negative Δ travel along the top track T_1 (i.e., they have a positive post-DEP x-coordinate), and vice versa. Three examples of position swapping from track T_1 to track T_2 and from track T_2 to track T_1 are shown in Fig. 4(c), one for each particle size, by means of overlays of consecutive snapshots. The probability density function (pdf) of the pre-DEP and post-DEP x-coordinate of particle centres are shown in Fig. 4(d) and (e), respectively, where populations are labelled according to the sign of the electrical metric Δ. Position swapping was successfully accomplished for 90% of particles, on a total of 400 particles (interfering particles[43] were discarded from the analysis).

Fig. 4 Particle position swapping experiment. (a) Scatter plot of the particle x-coordinate before the DEP actuation region against the amplitude relative difference Δ. (b) Scatter plot of the particle x-coordinate after the DEP actuation region against the amplitude relative difference Δ. (c) Examples of position swapping from the top track (T_1) to the bottom track (T_2) and vice versa. Overlays of consecutive image snapshots are shown. One example for each bead size is reported (small, 8 μm diameter; medium, 10 μm diameter; large, 12 μm diameter). (d) and (e) Histograms of the particle x-coordinate before and after the DEP actuation region, labelled according to the value of the amplitude relative difference Δ.

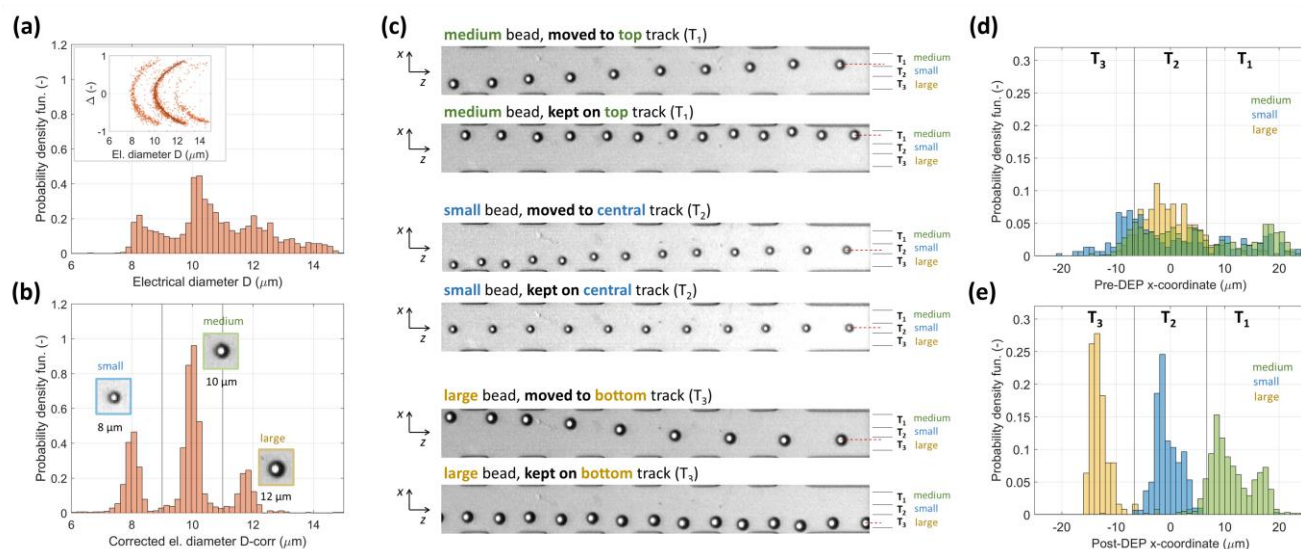### 4.3 Operation mode 2: size-based particle separation

To test the functionality of the system in an application-relevant task we considered particle separation by size (Fig. 1(c)). The premise for size-based particle separation is an accurate estimate of particle diameter. The latter is given by the electrical diameter corrected for position blurring, D-corr (eq. (3)). To obtain the relevant calibration coefficients (G, b, and c) an experiment was run without DEP actuation. A higher flow rate (5 μl/min) was used to quickly acquire many events and the recorded MIC signals were processed with the Matlab replica of the real time algorithm. Fig. 5(a) shows the pdf of the raw electrical diameter D (eq. (4)) for about 1800 events. As expected, positional dependence induces significant overlap among the three bead populations (8 μm, 10 μm, and 12 μm diameter). On the other hand, the three populations are well separated in the scatter plot of the amplitude relative difference Δ against the electric diameter D (inset in Fig. 5(a)). Calibration on the intermediate bead population yields the following coefficient values: $G = 9.5$ μm/μA$^{1/3}$, $b = 0.36$, and $c = 0.03$. The pdf of the corrected electrical diameter D-corr is shown in Fig. 5(b). After compensation for position blurring, the three populations can be easily identified by gating on D-corr with thresholds at 9 μm and 11 μm.

The size-based-separation operation mode (Fig. 1(c)) is implemented as follows: the particles are classified as small (D-corr < 9 μm), medium (9 μm ≤ D-corr < 11 μm), or large (D-corr ≥ 11 μm), and the DC voltages at the auxiliary outputs of the HF2IS are set to (5,5) V, (0,7) V, or (7,0) V, respectively. Upon multiplication by V^{SG}, they result in DEP voltages (V_1, V_2) of (7.5,7.5) V, (0,10.5) V, and (10.5,0) V, respectively. Accordingly, small particles are displaced towards the central track (T_2), medium particles are displaced towards the top track

(T_1), and large particles are displaced toward the bottom track (T_3).

Six examples are shown in Fig. 5(c), two for each particle size. For each bead type, a case where the particle is displaced and a case where the particle enters the DEP region already on the destination track are shown. The measured throughput was about 1.5 beads per second. The pdf of the x-coordinate of particle centres before and after the DEP actuation region are shown in Fig. 5(d) and (e), respectively, where populations are labelled according to size. While particles enter the DEP actuation region with random lateral position (pre-DEP x-coordinate), after the DEP actuation region they are clearly separated by size, with each population being focused on its destination track. Defining the extent of the central track (T_2) as $x \in [-7, 7]$ μm, 98% of 126 large beads, 93% of 621 medium beads, and 100% of 301 small beads were successfully displaced towards the correct destination track (i.e., 95% overall success rate).

### 4.4 Operation mode 3: sorting of a selected sequence of particles

Fig. 5 Size-based particle separation experiment. (a) Histogram of the electric diameter. In the inset, the scatter plot of the amplitude relative difference against the electric diameter is shown, along with the calibration curve (fitting the intermediate bead population). (b) Histogram of the electric diameter after compensation for position blurring. (c) Examples of particle separation by size. Overlays of consecutive image snapshots are shown. Two examples (moved to/kept on destination track) for each bead size are reported. (d) and (e) Histograms of the particle x-coordinate before and after the DEP actuation region, labelled according to the corrected electrical diameter.

Finally, we considered the task of sorting a selected sequence of particles, which finds application in the formation of aggregates of controlled size and composition.[29] As an example, we considered a sequence composed of one 12 μm bead followed by one 10 μm bead, periodically repeated.

The following control logic is accordingly implemented: if the incoming particle is the desired one (i.e., D-corr < 11 μm and the system is waiting for a 10 μm particle, or D-corr ≥ 11 μm and the system is waiting for a 12 μm particle), the DEP voltages (V_1, V_2) are set to $(0, 10.5)$ V, hence pushing the particle towards the top half of the microchannel (track T_1, target). If the incoming particle is out-of-sequence, the DEP voltages (V_1, V_2) are set to $(10.5, 0)$ V, thus pushing the particle towards the bottom half of the microchannel (track T_2, waste).

In this experiment, the sample concentration was 2.5×10^5 beads per mL and the measured throughput turned out to be about 0.5 beads/s. An exemplary portion of the recorded MIC signal is shown in Fig. 6. The incoming particle sequence is: 12 μm, 12 μm, 12 μm, 12 μm, 10 μm, 10 μm, 10 μm, 10 μm, 12 μm, 12 μm, 10 μm. Therefore, the first, fifth, nineth, and eleventh particles are moved to the target track (T_1), whereas the seven remaining ones are moved to the waste track (T_2). A video showing the sequence sorting process is included as Supplementary Material (Video S1). The video was acquired at 50 fps and is reproduced at 5 fps to better appreciate particle displacement (a few particle-empty frames were removed to reduce the overall video duration). Incoming particles, which arrive at arbitrary positions along channel width, are recognized in real-time as 12 μm or 10 μm beads by the MIC-sensing system and the adaptive DEP actuation system successfully sorts the desired particle sequence.

It is noticed that different particle sequence could be considered, also based on properties other than size.
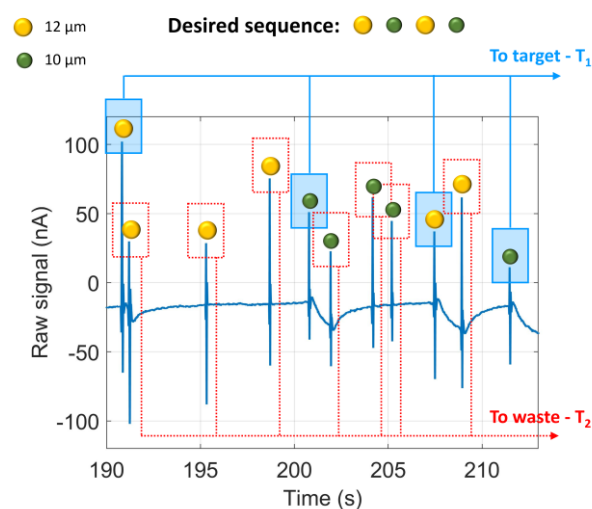
Fig. 6 Sorting of a selected particle sequence (i.e., 12 μm - 10 μm, periodic): exemplary portion of the raw signal recorded from the MIC sensing zone, with indication of the particle-generated signals and the corresponding particle types (10 μm or 12 μm diameter). Desired (to target) and out-of-sequence (to waste) particles are also highlighted.

5 Discussion

The proposed system combines MIC sensing and DEP actuation to achieve reconfigurable single-particle manipulation. A comparison with other platforms using MIC sensing and/or DEP actuation is included in the Supplementary Material (Table S1). The system throughput is about 1 particle per second, which is comparable to that of similar systems based on DEP manipulation[23,24]. Here, the throughput limitation comes from the time required by the DEP force to induce an effective particle displacement, which induces limitation on the flow rate. To allow higher throughput, higher DEP voltages can be considered, but this may require tailored electrode passivation strategies to avoid bubble formation. Moreover, the spatial extension of the actuation region limits the sample concentration, because only one particle at a time can be processed. As an improvement, the duration of the refractory state (S_2) could be tuned according to particle velocity (which is easily estimated from the signal peak-to-peak time[32]). Furthermore, an attractive possibility is the use of sequentially addressable DEP electrodes.[44]

To implement particle-position swapping, a sensing element able to establish in real-time the track of each incoming particle is needed. Hence, DEP actuation alone cannot implement particle position swapping. On the other hand, the use of DEP actuation alone for size-based separation of three particle populations has been previously reported in the literature (cf e.g. Refs[45,46] and the references therein). Typically, the DEP force is used to deviate the trajectory of pre-focused particles, and the amount of deviation increases with particle size. In contrast, our approach does not use particle pre-focusing, which simplifies the system, and allows more flexibility in the choice of the designated trajectory. For instance, we displaced small particles in the centre, medium particles on top, and large particles on bottom (i.e., particle position ordering does not follow particle size ordering).

To achieve size-based separation, the compensation procedure implemented to remove position blurring was fundamental to discriminate particles differing by 2 µm in their diameter (cf. Fig. 5(a) and (b)). As demonstrated in our previous work,[32] a 1 µm size resolution is also possible with the present MIC sensing system.

While MIC-sensing has been used here to characterize size and lateral position of particles, the technique can give electrical fingerprints that convey information on particle/cell geometric, dielectric, and mechanical properties too.[9] For instance, by using tailored electrode layouts, MIC sensing can discriminate particles by shape. A simple way to give shape-sensitivity to our system would be to use a MIC-sensing zone based on four coplanar electrodes arranged in a cross[41,47,48]. This modification would enable the implementation of a control logic based on particle shape and therefore shape-based particle separation.

As recently shown by Lipp et al.[28,29], the present DEP deviation system can be also used for cell manipulation. Moreover, expanding the channel width after the DEP-actuation region amplifies particle separation and five-way sorting (and possibly more) can be achieved.

Both MIC sensing and DEP actuation have been demonstrated for smaller particles, such as bacterial cells[49,50]. To work with smaller particles, an optimization of our system/setup would be needed, to keep a good signal-to-noise ratio of the impedance signals and a sufficiently high DEP force.

The proposed platform uses negative DEP to displace particles towards equilibrium positions. To allow efficient nDEP actuation, the real part of the Clausius-Mossotti factor of the manipulated object should be close to -0.5. Indeed, with the present experimental setup (medium conductivity of 0.9 S/m and electric field frequency of 400 kHz) the Clausius-Mossotti factor of 10 um polystyrene beads is -0.5. Simulations using the software MyDEP[51] show that comparable values are possible for biological cells (e.g., -0.48 for human T-cells), which is encouraging for future cell handling applications. On the other hand, the transition from beads to biological cells would require an optimization of the experimental setup (e.g., buffer osmolarity) to not alter cell physiological properties.

Overall, the present system holds promises as a selective particle and cell manipulation platform where several reconfigurable control logics could be implemented.

6 Conclusions

We reported an original all-electrical platform that combines MIC-sensing and DEP-actuation for precise and selective trajectory control of single flowing particles. As proof-of-concept applications we showed particle position swapping irrespective of particle size, size-based separation irrespective of particle incoming trajectory, and sorting of a selected sequence of particles. Nice features of the proposed platform are: (i) the label-free nature of the sensing approach, (ii) the contactless nature and multi-way sorting capabilities of the actuation mechanism, (iii) the simplicity of the layout, which is based on coplanar electrodes and does not require a particle focusing mechanism, and (iv) the reconfigurability of the control logic to achieve different sorting tasks. Moreover, both MIC-sensing and DEP-actuation are well-suited tools for biological cells, which encourages future studies towards cell handling applications.

Author Contributions

Conflicts of interest

There are no conflicts to declare.

Data availability

Journal Name ARTICLE

The data supporting this article have been included as part of the Supplementary Information.

References

1   S. Yang, Z. Tian, Z. Wang, J. Rufo, P. Li, J. Mai, J. Xia, H. Bachman, P.-H. Huang, M. Wu, C. Chen, L. P. Lee and T. J. Huang, *Nat Mater*, 2022, **21**, 540–546.

2   H. Afsaneh and R. Mohammadi, *Talanta Open*, 2022, 5.

3   P. Sajeesh and A. K. Sen, *Microfluid Nanofluidics*, 2014, 17.

4   M. Bayareh, *Chemical Engineering and Processing - Process Intensification*, 2020, 153.

5   S. Zhang, Y. Wang, P. Onck and J. den Toonder, *Microfluid Nanofluidics*, 2020, 24.

6   K. Cheng, J. Guo, Y. Fu and J. Guo, *Sens Actuators A Phys*, 2021, 322.

7   Y. Shen, Y. Yalikun and Y. Tanaka, *Sens Actuators B Chem*, 2019, **282**, 268–281.

8   T. Zhang, D. Di Carlo, C. T. Lim, T. Zhou, G. Tian, T. Tang, A. Q. Shen, W. Li, M. Li, Y. Yang, K. Goda, R. Yan, C. Lei, Y. Hosokawa and Y. Yalikun, *Biotechnol Adv*, 2024, 71.

9   C. Honrado, P. Bisegna, N. S. Swami and F. Caselli, *Lab Chip*, 2021, **21**, 22–54.

10   P. Li and Y. Ai, *Anal Chem*, 2021, **93**, 4108–4117.

11   J. Zhong, P. Li, M. Liang and Y. Ai, *Adv Mater Technol*, 2022, **7**, 2100906.

12   J. Zhong, M. Liang and Y. Ai, *Small Methods*, 2023, **7**, 2300089.

13   J. Zhong, M. Liang, Q. Tang and Y. Ai, *Mater Today Bio*, 2023, **19**, 100594.

14   M. P. Hughes, *Electrophoresis*, 2002, 23.

15   R. Pethig, *Dielectrophoresis: Theory, Methodology and Biological Applications, First Edition*, Wiley, 2017.

16   B. H. Lapizco-Encinas, *Electrophoresis*, 2019, 40.

17   G. R. Pesch and F. Du, *Electrophoresis*, 2021, 42.

18   G. R. Pesch, M. Lorenz, S. Sachdev, S. Salameh, F. Du, M. Baune, P. E. Boukany and J. Thöming, *Sci Rep*, 2018, **8**, 10480.

19   A. Y. L. Jiang, A. R. Yale, M. Aghaamoo, D.-H. Lee, A. P. Lee, T. N. G. Adams and L. A. Flanagan, *Biomicrofluidics*, 2019, **13**, 064111.

20   X. Huang, K. Torres-Castro, W. Varhue, A. Salahi, A. Rasin, C. Honrado, A. Brown, J. Guler and N. S. Swami, *Lab Chip*, 2021, **21**, 835–843.

21   K. Oshiro, Y. Wakizaka, M. Takano, T. Itoi, H. Ohge, K. Koba, K. Yarimizu, S. Fujiyoshi and F. Maruyama, *iScience*, 2022, **25**, 103776.

22   A. Rane, J. Jarmoshti, A.-B. Siddique, S. Adair, K. Torres-Castro, C. Honrado, T. W. Bauer and N. S. Swami, *Lab Chip*, 2024, **24**, 561–571.

23   B. de Wagenaar, S. Dekker, H. L. de Boer, J. G. Bomer, W. Olthuis, A. Van Den Berg and L. I. Segerink, *Lab Chip*, 2016, **16**, 1514–1522.

24   R. S. W. Thomas, P. D. Mitchell, R. O. C. Oreffo, H. Morgan and N. G. Green, *Electrophoresis*, 2019, **40**, 2718–2727.

25   F. Paratore, V. Bacheva, M. Bercovici and G. V. Kaigala, *Nat Rev Chem*, 2022, 6.

26   A. Lefevre, M. Gauthier, P. Bourgeois, A. Frelet-Barrand and A. Bolopion, *Lab Chip*, 2023, **23**, 3683–3693.

27   A. Lefevre, V. Gauthier, M. Gauthier and A. Bolopion, *IEEE/ASME Transactions on Mechatronics*, 2022, **27**, 4764–4773.

28   C. Lipp, L. Koebel, R. Loyon, A. Bolopion, L. Spehner, M. Gauthier, C. Borg, A. Bertsch and P. Renaud, *Lab Chip*, 2023, **23**, 3593–3602.

29   C. Lipp, L. Koebel, A. Bertsch, M. Gauthier, A. Bolopion and P. Renaud, *Front Bioeng Biotechnol*, 2022, **10**, 910578.

30   S. Wang, X. Wang, F. You and H. Xiao, *Micromachines (Basel)*, 2023, 14.

31   M. Kharboutly and M. Gauthier, in *Proceedings - IEEE International Conference on Robotics and Automation*, 2013.

32   F. Caselli, A. De Ninno, R. Reale, L. Businaro and P. Bisegna, *Sens Actuators B Chem*, 2018, **256**, 580–589.

33   R. Reale, A. De Ninno, L. Businaro, P. Bisegna and F. Caselli, *Lab Chip*, 2019, **19**, 1818–1827.

34   C. Honrado, J. S. McGrath, R. Reale, P. Bisegna, N. S. Swami and F. Caselli, *Anal Bioanal Chem*, 2020, **412**, 3835–3845.

35   H. Daguerre, M. Solsona, J. Cottet, M. Gauthier, P. Renaud and A. Bolopion, *Lab Chip*, 2020, **20**, 3665–3689.

36   N. Demierre, T. Braschler, P. Linderholm, U. Seger, H. Van Lintel and P. Renaud, *Lab Chip*, 2007, **7**, 355–365.

37   N. Demierre, T. Braschler, R. Muller and P. Renaud, *Sens Actuators B Chem*, 2008, **132**, 388–396.

38   R. Reale, A. De Ninno, L. Businaro, P. Bisegna and F. Caselli, *Electrophoresis*, 2019, **40**, 1400–1407.

39   F. Caselli and P. Bisegna, *IEEE Trans Biomed Eng*, 2016, **63**, 415–422.

40   M. D'Orazio, R. Reale, A. De Ninno, M. A. Brighetti, A. Mencattini, L. Businaro, E. Martinelli, P. Bisegna, A. Travaglini, F. Caselli, M. D'Orazio, R. Reale, A. De Ninno, M. A. Brighetti, D. A. Mencattini, L. Businaro, E. Martinelli, P. Bisegna, A. Travaglini and F. Caselli, *IEEE Trans Biomed Eng*, 2021, **69**, 921–931.

41   F. Caselli, M. Shaker, L. Colella, P. Renaud and P. Bisegna, *J. Microelectromech. Syst.*, 2014, **23**, 785–794.

42   T. B. Jones, *Electromechanics of Particles*, Cambridge University Press, 1995.

43   F. Caselli, A. De Ninno, R. Reale, L. Businaro and P. Bisegna, *IEEE Trans Biomed Eng*, 2020, **68**, 340–349.

44   A. Isozaki, Y. Nakagawa, M. H. Loo, Y. Shibata, N. Tanaka, D. L. Setyaningrum, J.-W. Park, Y. Shirasaki, H. Mikami, D. Huang, H. Tsoi, C. T. Riche, T. Ota, H. Miwa, Y. Kanda, T. Ito, K. Yamada, O. Iwata, K. Suzuki, S. Ohnuki, Y. Ohya, Y. Kato, T. Hasunuma, S. Matsusaka, M. Yamagishi, M. Yazawa, S. Uemura, K. Nagasawa, H. Watarai, D. Di Carlo and K. Goda, *Sci Adv*, 2020, **6**, eaba6712.

45   R. Derakhshan, A. Bozorgzadeh and A. Ramiar, *J Chromatogr A*, 2023, **1702**, 464079.

46   R. Derakhshan, A. Ramiar and A. Ghasemi, *Analyst*, 2022, **15**, 5395–5408.

47   M. Shaker, L. Colella, F. Caselli, P. Bisegna and P. Renaud, *Lab Chip*, 2014, **14**, 2548–2555.

48   R. Reale, A. De Ninno, T. Nepi, P. Bisegna and F. Caselli, *IEEE Trans Biomed Eng*, 2022, 1–9.

49   C. Troiano, A. De Ninno, B. Casciaro, F. Riccitelli,
        Y. Park, L. Businaro, R. Massoud, M. L. Mangoni,
        P. Bisegna, L. Stella and F. Caselli, *ACS Sens*,
        2023, **8**, 2572–2582.

50   R. Hamada, H. Takayama, Y. Shonishi, L. Mao, M.
        Nakano and J. Suehiro, *Sens Actuators B Chem*,
        2013, **181**, 439–445.

51   J. Cottet, O. Fabregue, C. Berger, F. Buret, P.
        Renaud and M. Frénéa-Robin, *Biophys J*, 2019,
        116, 12–18.